Science
AAAS

Superelastic Effect in Polycrystalline Ferrous Alloys

T. Omori, *et al.*

Science **333**, 68 (2011);
DOI: 10.1126/science.1202232

Science (print ISSN 0036-8075; online ISSN 1095-9203) is published weekly, except the last week in December, by the American Association for the Advancement of Science, 1200 New York Avenue NW, Washington, DC 20005.

Superelastic Effect in Polycrystalline Ferrous Alloys

T. Omori,* K. Ando, M. Okano, X. Xu, Y. Tanaka, I. Ohnuma, R. Kainuma, K. Ishida

In superelastic alloys, large deformation can revert to a memorized shape after removing the stress. However, the stress increases with increasing temperature, which limits the practical use over a wide temperature range. Polycrystalline Fe-Mn-Al-Ni shape memory alloys show a small temperature dependence of the superelastic stress because of a small transformation entropy change brought about by a magnetic contribution to the Gibbs energies. For one alloy composition, the superelastic stress varies by 0.53 megapascal/°C over a temperature range from −196 to 240°C.

Since shape memory behavior was discovered in Au-Cd alloys (*1*), many shape memory alloy systems, such as Ti-Ni, Cu-Al-Ni, Ni-Mn-Ga, and Ni-Co-Mn-In alloys, have been reported (*2*–*4*). In contrast to metallic materials with elastic limits of about 0.2%, Ti-Ni alloys exhibit a large recoverable strain of up to 8% and are used in engineering and medical fields (*5*). Superelasticity is caused by a reversible phase transformation between the parent phase, stable under no stress, and the martensite phase, stabilized by stress. The critical stress for stress-induced martensitic transformations, σ_c, hereafter called superelastic stress, which corresponds to an effective yield stress in superelastic behavior, increases with increasing temperature T in agreement with the Clausius-Clapeyron relation (*6*):

$$\frac{d\sigma_c}{dT} = -\frac{\Delta S}{\varepsilon \cdot V_m} \quad (1)$$

where ΔS is the molar entropy difference between the parent and martensite phases, ε is the strain caused by the phase transformation, and V_m is the molar volume. The rate of increase in Ti-Ni alloys is about 6 MPa °C^{-1}.

We recently reported that the ternary alloy $Fe_{49}Mn_{36}Al_{15}$ undergoes a martensitic transformation from the α parent phase with a body-centered cubic (bcc: A2) structure to a γ′ martensite phase with a face-centered cubic (fcc: A1) structure (*7*); the prime in this phase notation represents a martensite phase. The sequence of the phase transformation from the α phase (high-temperature parent phase) to the γ′ phase (low-temperature or stress-induced phase) in the Fe-Mn-Al alloy is unusual, because most Fe alloys exhibit a martensitic transformation from a γ phase with the A1 structure to a α′ phase with the A2 or body-centered tetragonal (bct) structure. It is known that the superelastic behavior is usually attributed to a thermoelastic martensitic transformation, in which a martensite plate grows and shrinks upon cooling and heating, respectively (*2*). However, most Fe-based alloys, including the Fe-Mn-Al, have a nonthermoelastic martensitic transformation with no reversibility in the microstructure and exhibit no superelasticity. Thermoelastic martensitic transformations have been reported in alloy systems with fully or partially ordered structures, such as Ti-Ni with the CsCl-type ordered bcc (B2) structure and Fe-Ni-Co-Ti (*8*) and Fe-Ni-Co-Al (*9*) alloys with coherent precipitates, Ni_3Ti and Ni_3Al, having a $L1_2$ structure in the γ phase. It is known that the B2 phase exists over a wide concentration range in Ni-Mn-Al system (*10*) and that a phase separation of the A2 and B2 phases occurs by low-temperature aging in Fe-Ni-Al (*11*). On the basis of the information, we tried adding a range of Ni to the Fe-Mn-Al alloy, and $Fe_{43.5}Mn_{34}Al_{15}Ni_{7.5}$ superelastic alloy with nanosized particles of the B2 ordered phase in the A2 disordered matrix phase (fig. S2) was obtained.

The magnetization versus temperature (*M*-*T*) of $Fe_{43.5}Mn_{34}Al_{15}Ni_{7.5}$ measured in a magnetic field of 0.05 T is shown in Fig. 1A for an as-solution-treated specimen and in Fig. 1B for a specimen aged at 200°C for 15 min (*12*). For both specimens, an abrupt decrease and increase in magnetization because of the martensitic transformation were detected in both cooling and heating cycles. The transformation process in Fig. 1A was found to have a temperature hysteresis, defined as $T_{Af} - T_{Ms}$ or $T_{As} - T_{Mf}$, of 150°C, where T_{Ms} and T_{Mf} are the martensitic transformation starting and finishing temperatures and T_{As} and T_{Af} the reverse transformation starting and finishing temperatures. Although temperature hysteresis in thermoelastic transformations is normally less than ~100°C (*2*, *13*), the martensitic transformation in the $Fe_{43.5}Mn_{34}Al_{15}Ni_{7.5}$ alloy is thermoelastic because growth and shrinkage of martensite plates are observed upon cooling and heating, respectively, as shown in Fig. 1B. The $Fe_{43.5}Mn_{34}Al_{15}Ni_{7.5}$ alloy shows an abnormal magnetic change from a ferromagnetic parent phase to a weak magnetic martensite phase during cooling. Further aging at 200°C for 3 hours causes the martensitic transformation to be suppressed, and the *M*-*T* curve for the specimen aged at 200°C for 6 hours is shown in Fig. 1C. From the change of transformation behavior with aging, it is apparent that the martensitic transformation temperatures gradually decrease after aging at 200°C. In order to clarify the magnetic features of the martensite phase, we measured magnetization of a specimen having a fully martensitic structure. Figure 1D shows the magnetization-versus-temperature curve obtained in a magnetic field of 10 kOe for a specimen with a single martensite phase obtained by a ~80% reduction in thickness

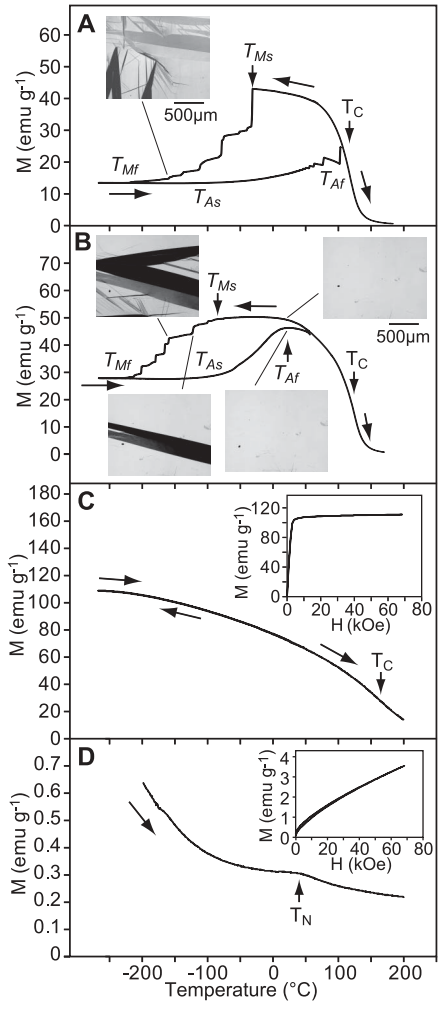

Fig. 1. Thermomagnetization curves of $Fe_{43.5}Mn_{34}Al_{15}Ni_{7.5}$. (**A**) Curve of the as-solution-treated sample in a magnetic field of 0.5 kOe. (Inset) Optical micrograph taken at −160°C. emu indicates electromagnetic unit. (**B**) Curve of the sample aged at 200°C for 15 min in a magnetic field of 0.5 kOe. (Insets) Optical micrographs taken at 20°C, −120°C, and −160°C in the cooling process and at 20°C in the heating process. (**C**) Curve of the sample aged at 200°C for 6 hours in a magnetic field of 10 kOe. (Inset) The magnetization versus magnetic field measured at 4.2 K. (**D**) Curve of the sample aged at 200°C for 6 hours and subsequently cold-rolled at a reduction rate of 80%, where the cold rolling was carried out in order to obtain the martensite phase. A magnetic field of 10 kOe was applied. (Inset) The magnetization versus magnetic field at 4.2 K. The Curie temperature of each specimen was determined to be 117°C, 124°C, and 165°C for (A), (B), and (C), respectively, and the Néel temperature is 40°C in (D).

Department of Materials Science, Graduate School of Engineering, Tohoku University, 6-6-02 Aoba-yama, Sendai 980-8579, Japan.

*To whom correspondence should be addressed. E-mail: omori@material.tohoku.ac.jp

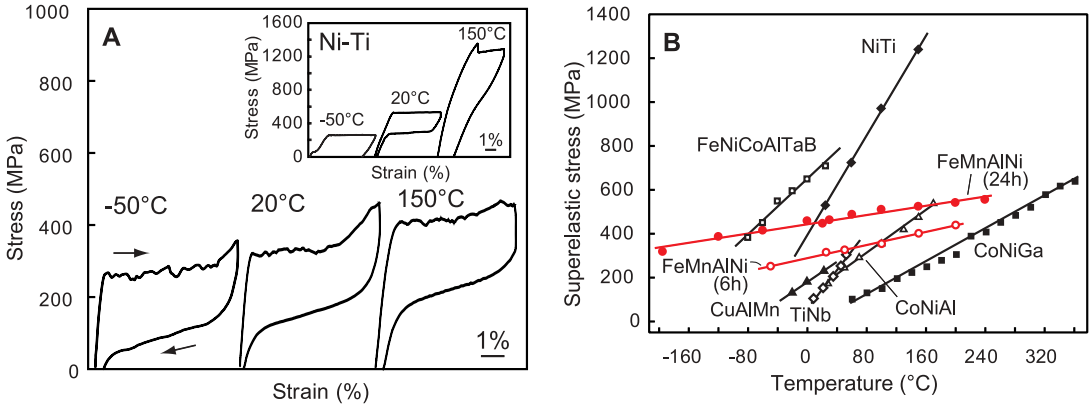

Fig. 2. Superelastic properties of Fe-Mn-Al-Ni and its temperature dependence. (**A**) Stress-strain curves of $Fe_{43.5}Mn_{34}Al_{15}Ni_{7.5}$ aged at 200°C for 6 hours at various temperatures in a tensile test. (Inset) The superelasticity of commercial $Ti_{49.98}Ni_{50.02}$. Compared with Ti-Ni, the stress level in Fe-Mn-Al-Ni is insensitive to temperature. (**B**) Superelastic stress as a function of temperature in $Fe_{43.5}Mn_{34}Al_{15}Ni_{7.5}$ polycrystalline alloy and conventional $Ti_{49.98}Ni_{50.02}$, $Fe_{40.95}Ni_{28}Co_{17}Al_{11.5}Ta_{2.5}B_{0.05}$, $Cu_{71.9}Al_{16.6}Mn_{9.3}Ni_2B_{0.2}$, $Ti_{74}Nb_{26}$, and $Co_{37.6}Ni_{32.9}Al_{29.5}$ polycrystalline alloys and $Co_{49}Ni_{21}Ga_{30}$ single crystal. The stresses are in tension except for Co-Ni-Al and Co-Ni-Ga in compression.

after cold rolling. It was found that the martensite phase became antiferromagnetic below a Néel temperature, T_N, of 40°C. This result means that the martensitic transformation occurring at temperatures below 40°C is from a ferromagnetic to an antiferromagnetic state, which is similar to the magnetic transformation reported in FeRh alloy (*14*). Furthermore, in the as-solution-treated sample a large amount of parent phase remains at –160°C (Fig. 1A, inset), and the martensitic transformation does not apparently complete even by cooling to 4.2 K.

In order to examine ductility and superelasticity of the $Fe_{43.5}Mn_{34}Al_{15}Ni_{7.5}$ alloy, we carried out tensile tests at several temperatures. The stress-strain curves at –50°C, 20°C, and 150°C for the alloy aged at 200°C for 6 hours are shown in Fig. 2A. The alloy exhibits excellent ductility with a fracture tensile strain of over 8% and pseudoelastic behavior with a recoverable strain of over 5%. This is obtained despite no thermal martensitic transformation on cooling (Fig. 1C). We conducted in situ observation of the microstructure during the tensile testing to decide the origin of this pseudoelastic behavior. It was confirmed that the stress-induced martensite (SIM) plates appear upon loading and disappear upon unloading (fig. S4) and that this pseudoelastic behavior is superelasticity resulting from SIM transformation. The superelasticity depends on the relative grain size d/t and d/w, where d, t, and w are the mean grain diameter, thickness, and width of the sheet specimen, respectively, and the superelastic strain increases with increasing d/t and d/w as shown in fig. S5. The d/w in Fig. 2 is about 3.8.

The stress-strain curves obtained at different temperatures for the $Fe_{43.5}Mn_{34}Al_{15}Ni_{7.5}$ alloy are very similar to one another in contrast to those for a commercial Ti-Ni alloy (Fig. 2A). The superelastic stresses of the $Fe_{43.5}Mn_{34}Al_{15}Ni_{7.5}$ alloys are plotted with those of other polycrystalline superelastic alloys in Fig. 2B. The $Fe_{43.5}Mn_{34}Al_{15}Ni_{7.5}$ alloy exhibits superelasticity over a very wide temperature range from –196° to 240°C (i.e., the temperature window is about 440°C at least) for the one composition with very small temperature dependence of superelastic stress. It can be seen that the slopes ($=d\sigma_c/dT$) of the plots for the Fe-Mn-Al-Ni specimens aged at 200°C for 6 and 24 hours are 0.74 MPa °C^{-1} and 0.53 MPa °C^{-1}, respectively. Furthermore the temperature dependences are smaller, roughly by one order of magnitude, than those in conventional superelastic alloys, Ti-Ni (5.7 MPa °C^{-1}), Fe-Ni-Co-Al-Ta-B (3.1 MPa °C^{-1}), Cu-Al-Mn [2.4 MPa °C^{-1} (*15*)], Ti-Nb [4.4 MPa °C^{-1} (*16*)], Co-Ni-Al [2.5 MPa °C^{-1} (*17*)], and Co-Ni-Ga [1.9 MPa °C^{-1} (*17*)] (table S1). The temperature-insensitive superelasticity has also been obtained in an $Fe_{45.5}Mn_{32}Al_{15}Ni_{7.5}$ alloy with higher superelastic stress by about 150 MPa. The ΔS can be calculated by Eq. 1 using the experimental value $d\sigma_c/dT$ and the molar volume V_m when we know the ε. However, it is difficult to determine the ε in the polycrystalline specimen in Fig. 2. Therefore, we conducted a tensile test at various temperatures in an $Fe_{43.5}Mn_{34}Al_{15}Ni_{7.5}$ single crystal, and the ΔS was determined as being –0.43 J mol^{-1} K^{-1} by using the experimental results of $d\sigma_c/dT$ = 0.60 MPa °C^{-1} and ε = 0.097 (fig. S1) and $V_m = 7.366 \times 10^{-6}$ m^3 mol^{-1}.

According to Eq. 1, the temperature dependence of superelastic stress is proportional to ΔS under fixed ε and V_m. We discuss the temperature-insensitive superelasticity from a thermodynamic viewpoint by using the phenomenological CALPHAD (calculation of phase diagrams) method. Because the calculation for the quaternary two-phase alloys is complicated and Ni content in the matrix is expected to be low resulting from the precipitation of the B2 (NiAl) phase, we con-

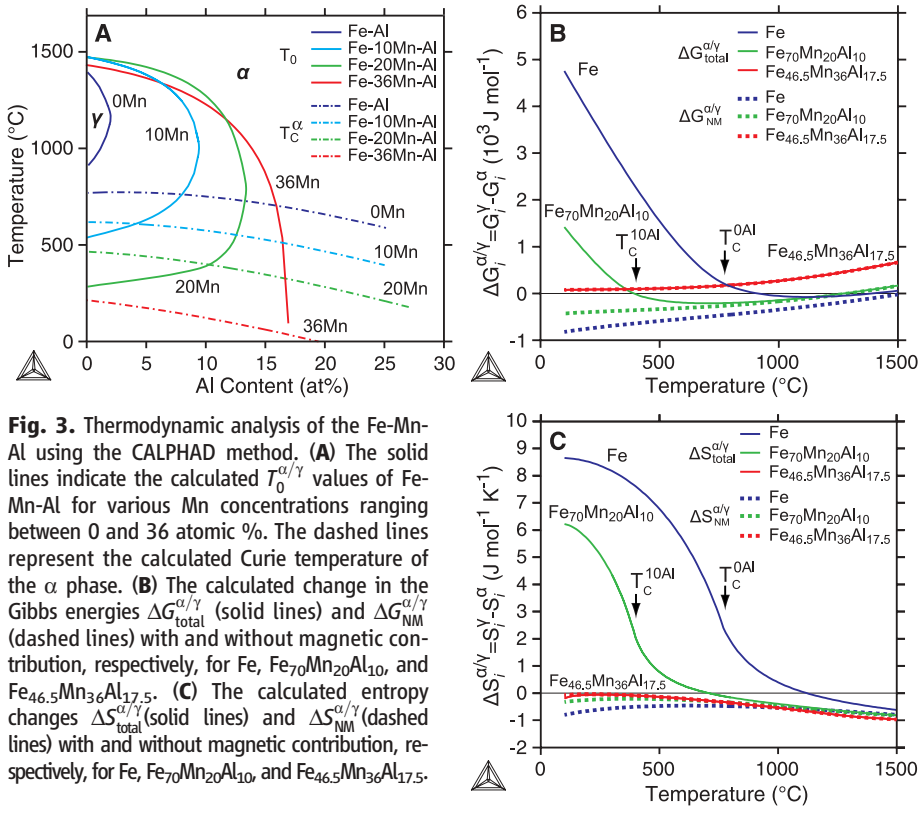

Fig. 3. Thermodynamic analysis of the Fe-Mn-Al using the CALPHAD method. (**A**) The solid lines indicate the calculated $T_0^{\alpha/\gamma}$ values of Fe-Mn-Al for various Mn concentrations ranging between 0 and 36 atomic %. The dashed lines represent the calculated Curie temperature of the α phase. (**B**) The calculated change in the Gibbs energies $\Delta G_{total}^{\alpha/\gamma}$ (solid lines) and $\Delta G_{NM}^{\alpha/\gamma}$ (dashed lines) with and without magnetic contribution, respectively, for Fe, $Fe_{70}Mn_{20}Al_{10}$, and $Fe_{46.5}Mn_{36}Al_{17.5}$. (**C**) The calculated entropy changes $\Delta S_{total}^{\alpha/\gamma}$ (solid lines) and $\Delta S_{NM}^{\alpha/\gamma}$ (dashed lines) with and without magnetic contribution, respectively, for Fe, $Fe_{70}Mn_{20}Al_{10}$, and $Fe_{46.5}Mn_{36}Al_{17.5}$.

sidered the thermodynamic quantities of the α (A2) and γ (A1) phases for the Fe-Mn-Al ternary system (*18*) rather than for Fe-Mn-Al-Ni. Figure 3A shows the equilibrium temperature $T_0^{\alpha/\gamma}$ lines calculated for Fe-Mn-Al alloys with various Mn concentrations, together with the Curie temperatures T_C^{α} of the α phase. $T_0^{\alpha/\gamma}$ is the temperature at which the Gibbs energies of the α and γ phases are equal and approximately corresponds to $T_0^{\alpha/\gamma} \approx (T_{Ms} + T_{Af})/2$ in thermoelastic martensitic transformation of a single-crystal specimen (*19*). From Fig. 3A it can be seen that the α phase is substantially stabilized near T_C^{α}, forming so-called γ loops, up to 30 atomic % Mn, where the conventional γ/α′ martensitic transformation takes place on cooling from the γ to the α region. With increasing Mn content and for Al content above 15%, T_C^{α} decreases to near room temperature and the γ loop diminishes, as seen for the ^{36}Mn alloy. In this condition, a diffusionless martensitic transformation can take place from the α to the γ′ phase because it can go through the $T_0^{\alpha/\gamma}$ line at low temperatures.

Figure 3, B and C, shows the differences in Gibbs energy, $\Delta G_{total}^{\alpha/\gamma}$ and $\Delta G_{NM}^{\alpha/\gamma}$, and the differences in entropy, $\Delta S_{total}^{\alpha/\gamma}$ and $\Delta S_{NM}^{\alpha/\gamma}$, between the α and γ phases calculated for pure Fe, $Fe_{70}Mn_{20}Al_{10}$, and $Fe_{46.5}Mn_{36}Al_{17.5}$ alloys, where $\Delta G_{total}^{\alpha/\gamma}$ and $\Delta S_{total}^{\alpha/\gamma}$ are defined as

$$G_{total}^{\alpha} = G_{NM}^{\alpha} + \Delta G_{mag}^{\alpha}, \quad G_{total}^{\gamma} = G_{NM}^{\gamma} + \Delta G_{mag}^{\gamma} \tag{2}$$

$$\Delta G_{NM}^{\alpha/\gamma} = G_{NM}^{\gamma} - G_{NM}^{\alpha} \tag{3}$$

$$\Delta G_{mag}^{\alpha/\gamma} = \Delta G_{mag}^{\gamma} - \Delta G_{mag}^{\alpha} \tag{4}$$

$$\begin{aligned}\Delta G_{total}^{\alpha/\gamma} &= G_{total}^{\gamma} - G_{total}^{\alpha} \\ &= G_{NM}^{\gamma} - G_{NM}^{\alpha} + \Delta G_{mag}^{\gamma} - \Delta G_{mag}^{\alpha} \\ &= \Delta G_{NM}^{\alpha/\gamma} + \Delta G_{mag}^{\alpha/\gamma}\end{aligned} \tag{5}$$

$$S_{total}^{\alpha} = S_{NM}^{\alpha} + \Delta S_{mag}^{\alpha}, \quad S_{total}^{\gamma} = S_{NM}^{\gamma} + \Delta S_{mag}^{\gamma} \tag{6}$$

$$\Delta S_{NM}^{\alpha/\gamma} = S_{NM}^{\gamma} - S_{NM}^{\alpha} \tag{7}$$

$$\Delta S_{mag}^{\alpha/\gamma} = \Delta S_{mag}^{\gamma} - \Delta S_{mag}^{\alpha} \tag{8}$$

$$\begin{aligned}\Delta S_{total}^{\alpha/\gamma} &= S_{total}^{\gamma} - S_{total}^{\alpha} \\ &= S_{NM}^{\gamma} - S_{NM}^{\alpha} + \Delta S_{mag}^{\gamma} - \Delta S_{mag}^{\alpha} \\ &= \Delta S_{NM}^{\alpha/\gamma} + \Delta S_{mag}^{\alpha/\gamma}\end{aligned} \tag{9}$$

where Gibbs energy, G_i^{ϕ}, and entropy, S_i^{ϕ}, refer to the ϕ phase. Here, the subscript *i* is either mag or NM and indicates whether in the calculation the magnetic term has been included or excluded, respectively. As shown by the solid lines of Fig. 3B, $\Delta G_{total}^{\alpha/\gamma}$ of pure Fe and of $Fe_{70}Mn_{20}Al_{10}$ abruptly increases with decreasing temperature in the region below T_C^{α} of the α phase. However, $\Delta G_{NM}^{\alpha/\gamma}$ monotonically decreases, as demonstrated by the dashed lines of Fig. 3B. This means that the ferromagnetism of the α phase strongly affects phase stability and that the bcc "ferrite" phase never appears unless there is a magnetic contribution, as pointed out by Zener (*20*). The magnetic contribution to $\Delta S_{total}^{\alpha/\gamma}$ of pure Fe and $Fe_{70}Mn_{20}Al_{10}$ is very large (Fig. 3C). Decreasing T_C^{α} of the α phase, by adding both Mn and Al, reduces the effect of the magnetic term in $\Delta G_{mag}^{\alpha/\gamma}$ and $\Delta S_{mag}^{\alpha/\gamma}$ (Fig. 3, A to C). In $Fe_{46.5}Mn_{36}Al_{17.5}$, which is selected as a ternary alloy with phase stability and magnetic properties similar to those of the $Fe_{43.5}Mn_{34}Al_{15}Ni_{7.5}$ alloy (Fig. 1), the magnetic contribution is further reduced, the differences between $\Delta G_{total}^{\alpha/\gamma}$ and $\Delta G_{NM}^{\alpha/\gamma}$ and between $\Delta S_{total}^{\alpha/\gamma}$ and $\Delta S_{NM}^{\alpha/\gamma}$ are hardly observed, and the entropy change $\Delta S_{total}^{\alpha/\gamma}$ becomes close to zero. Besides the ferromagnetism of the α phase, the antiferromagnetism of the γ phase is also important, and the magnetic effect of the antiferromagnetism (*21*, *22*) should be taken into account to obtain the small $\Delta S_{total}^{\alpha/\gamma}$. The result calculated for $Fe_{46.5}Mn_{36}Al_{17.5}$ (Fig. 3C) is comparable to the ΔS (= –0.43 J mol^{-1} K^{-1}) for $Fe_{43.5}Mn_{34}Al_{15}Ni_{7.5}$ evaluated from Eq. 1. The ΔS of Fe-Mn-Al-Ni is smaller by one order of magnitude than the –4.37 J mol^{-1} K^{-1} found in Ti-Ni (*23*), the –6.28 J mol^{-1} K^{-1} in Fe-Ni (*24*), and those in other superelastic alloys (table S1). The temperature-insensitive superelastic effect is considered to be strongly related to the magnetic contribution to the thermodynamic quantities. Because the driving force for thermal martensitic transformation ΔG is given with supercooling ΔT by $\Delta G \approx \Delta S \cdot \Delta T$ and thermal hysteresis is inversely proportional to ΔS, the large thermal hysteresis shown in Fig. 1, A and B, is apparently brought about by the small ΔS.

A small temperature dependence of superelasticity over a wide temperature range is very important for practical applications because structural and functional materials are, in most cases, subjected to change in temperature. Figure 4 shows the temperature ranges in which the superelasticity can be obtained and the temperature width giving the change of superelastic stress of 100 MPa for the commercial Ti-Ni, Fe-Ni-Co-Al, and Cu-Al-Mn and the present Fe-Mn-Al-Ni alloy. The temperature of matter in space (Earth's orbit) changes from about –150°C in the shade to about 120°C under sunlight, and for most automotive applications operation at temperatures ranging from about –50 to 150°C is required (Fig. 4). Ti-Ni applications are limited to temperatures lower than about 80°C. This means that Fe-Mn-Al-Ni has potential for use as a superelastic alloy in severe environments, such as high-integrity seals, joints, and controls of a broad variety in automobile, aeroplane, and space systems. Recently, superelastic alloys have attracted much attention for seismic applications because they can exhibit recentering and damping capabilities against strong earthquakes (*25*, *26*). However, high cost because of raw materials and the forming and machining of Ti-Ni is an obstacle for the application of superelastic alloys, and its implementation has been limited to a few historic buildings (*27*). Because the Fe-Mn-Al-Ni alloy is composed of common metals and has high workability as well as small temperature dependence, it offers great promise as a candidate for large-scale applications such as seismic dampers and isolators.

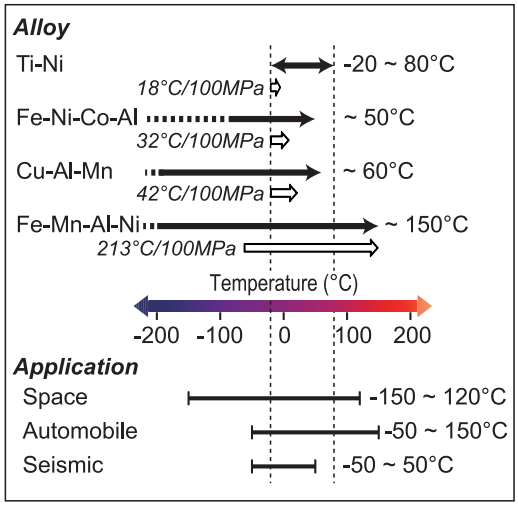

Fig. 4. Operational temperature range of polycrystalline superelastic alloys. The arrows indicate the temperature regions in which superelasticity can be obtained, and the temperature width over which the superelastic stress changes by 100 MPa is also shown.

References and Notes

1. A. Ölander, *J. Am. Chem. Soc.* **56**, 3819 (1932).
2. K. Otsuka, C. M. Wayman, in *Shape Memory Materials*, K. Otsuka, C. M. Wayman, Eds. (Cambridge Univ. Press, Cambridge, 1998), pp. 1–48.
3. T. Kakeshita, K. Ullakko, *MRS Bull.* **27**, 105 (2002).
4. R. Kainuma *et al.*, *Nature* **439**, 957 (2006).
5. T. W. Duerig, K. N. Melton, D. Stöckel, C. M. Wayman, *Engineering Aspects of Shape Memory Alloys* (Butterworth-Heinemann, London, 1990).

6. P. Wollants, M. De Bonte, J. R. Roos, *Z. Metallk.* **70**, 113 (1979).
7. K. Ando, T. Omori, I. Ohnuma, R. Kainuma, K. Ishida, *Appl. Phys. Lett.* **95**, 212504 (2009).
8. T. Maki, K. Kobayashi, M. Minato, I. Tamura, *Scr. Metall.* **18**, 1105 (1984).
9. Y. Tanaka *et al.*, *Science* **327**, 1488 (2010).
10. R. Kainuma, M. Ise, K. Ishikawa, I. Ohnuma, K. Ishida, *J. Alloy. Comp.* **269**, 173 (1998).
11. S. M. Hao, T. Takayama, K. Ishida, T. Nishizawa, *Metall. Trans.* **15**, 1819 (1984).
12. Materials and methods are available as supporting material on *Science* Online.
13. T. Maki, in *Shape Memory Materials*, K. Otsuka, C. M. Wayman, Eds. (Cambridge Univ. Press, Cambridge, 1998), pp. 117–132.
14. L. Muldawer, F. de Bergevin, *J. Chem. Phys.* **35**, 1904 (1961).
15. Y. Sutou, N. Koeda, T. Omori, R. Kainuma, K. Ishida, *Acta Mater.* **57**, 5759 (2009).
16. H. Y. Kim, S. Hashimoto, J. I. Kim, H. Hosoda, S. Miyazaki, *Mater. Trans.* **45**, 2443 (2004).
17. J. Ma, I. Karaman, R. D. Noebe, *Int. Mater. Rev.* **55**, 257 (2010).
18. R. Umino *et al.*, *J. Phase Equilibria Diffus.* **27**, 54 (2006).
19. H. C. Tong, C. M. Wayman, *Acta Metall.* **22**, 887 (1974).
20. C. Zener, *J. Met.* **7**, 619 (1955).
21. S. S. Yan *et al.*, *Solid State Commun.* **54**, 831 (1985).
22. G. A. Pérez Alcazar, E. Galvão da Silva, C. Paduani, *Hyperfine Interact.* **66**, 221 (1991).
23. W. Tang, R. Sandström, Z. G. Wei, S. Miyazaki, *Metall. Mater. Trans. A Phys. Metall. Mater. Sci.* **31**, 2423 (2000).
24. C. L. Magee, R. G. Davies, *Acta Metall.* **20**, 1031 (1972).
25. E. J. Graesser, F. A. Cozzarelli, *J. Eng. Mech.* **117**, 2590 (1991).
26. M. Dolce, D. Cardone, R. Marnetto, *Earthquake Eng. Struct. Dynam.* **29**, 945 (2000).
27. A. Abbott, *Nature* **414**, 572 (2001).

Acknowledgments: The authors are grateful to K. R. A Ziebeck, Cavendish Laboratory, University of Cambridge, for help in critical reading. This work was supported by the Grants-in-Aid for Scientific Research from Japan Society for the Promotion of Science and by the Global Center of Excellence Program "Materials Integration (International Center of Education and Research), Tohoku University," Ministry of Education, Culture, Sports, Science, and Technology. A patent application has been filed on the materials, including the alloy presented herein.

Supporting Online Material

www.sciencemag.org/cgi/content/full/333/6038/68/DC1
Materials and Methods
SOM Text
Figs. S1 to S6
Table S1
References (*28*–*41*)

27 December 2010; accepted 13 May 2011
10.1126/science.1202232

Solvated Electrons in High-Temperature Melts and Glasses of the Room-Temperature Stable Electride $[Ca_{24}Al_{28}O_{64}]^{4+}\cdot 4e^-$

Sung Wng Kim,[1] Terumasa Shimoyama,[2] Hideo Hosono[1,2]

Solvated electrons in alkali metal-ammonia solutions have attracted attention as a prototype electronic conductor and chemical reducing agent for over a century. However, solvated electrons have not been realized in a high-temperature melt or glass of an oxide system to date. We demonstrated the formation of persistent solvated electrons in both a high-temperature melt and its glass by using the thermally stable electride $[Ca_{24}Al_{28}O_{64}]^{4+}\cdot 4e^-$ (C12A7:e^-) and controlling the partial pressure of oxygen. The electrical and structural properties of the resulting melt and glass differ from those of the conventional C12A7:O^{2-} oxide, exhibiting metallic and hopping conduction, respectively, and a glass transition temperature that is ~160 kelvin lower than that of C12A7:O^{2-} glass. Solvated electrons reside in cage structures in C12A7:e^- and form a diamagnetic paired state.

Solvated electrons in alkali metal-ammonia solution have been a diverse stem for scientific and applied researches (*1*). Furthermore, alkali metal-amine solutions containing solvated electrons can be condensed into ionic solids, known as electrides, in which electrons are trapped in well-defined structural cavities and/or channels in matrices (*2*). Organic electrides can be created in which organic complexants, such as crown ethers, bind electrons, but these compounds are thermally unstable (*2*). This drawback provoked the development of thermally stable electrides based on inorganic compounds, such as calcium aluminum oxide ($12CaO\cdot 7Al_2O_3$, abbreviated as C12A7:O^{2-}). In this compound, O^{2-} is a caged species that compensates for the positive charge of the ~0.4-nm cage, and an electride can be formed by displacing this anion (*3*, *4*). The caged electrons are protected from air and moisture even near room temperature (RT) because of the small size of the windows (diameters of ~0.1 nm) connecting the cages.

C12A7:e^- can be synthesized by means of various chemical and physical processes. We reported that strongly reduced C12A7:O^{2-} melt crystallizes to form C12A7:e^- and that single crystals of C12A7:e^- can be grown from polycrystalline C12A7:e^- by the floating zone (FZ) melting method under a strongly reducing atmosphere (*5*, *6*). These findings imply that the electrons persist in the cages just below melting point (T_m) under a strongly reducing atmosphere. Because

[1]Frontier Research Center, Tokyo Institute of Technology, Post Office Box S2-13, 4259 Nagatsuta, Midori-ku, Yokohama 226-8503, Japan. [2]Materials and Structures Laboratory, Tokyo Institute of Technology, Post Office Box R3-1, 4259 Nagatsuta, Midori-ku, Yokohama 226-8503, Japan.

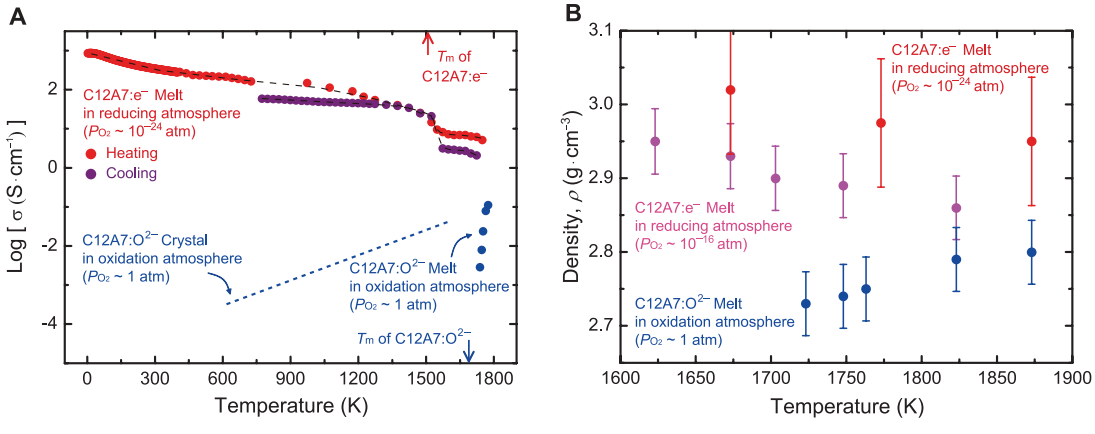

Fig. 1. (**A**) The temperature dependence of σ of C12A7:e^- and C12A7:O^{2-} melts. The σ of C12A7:e^- melt decreases as the temperature increases, showing metallic conduction. In contrast, a melt of the mother compound, C12A7:O^{2-} oxide, shows ionic conduction. Upon melting, the σ of C12A7:e^- electride decreases to several siemens, which is an order of magnitude lower than that of the crystalline electride just below T_m. The sudden decrease in the σ of C12A7:O^{2-} on melting is ascribed to the disappearance of free O^{2-} ions accommodated in the cages because of the collapse of the three-dimensional network of sub-nanometer-sized cages that serve as the conduction pathway for oxide ions. The activation of ionic conduction in the C12A7:O^{2-} melt (6.3 eV) is related to viscosity (*19*), implying that dissociation of O^{2-} ions from the polymerized network structures determines both the rate of ionic conduction and viscous flow. (**B**) Density of C12A7:e^- and C12A7:O^{2-} melts as a function of temperature. All data were acquired during heating. The red and pink circles represent the densities of C12A7:e^- melts measured under PO_2 ~10^{-24} and ~10^{-16} atm, respectively. The error range was ±3% for the red and ±2% for the pink and blue data points.